

Designing polymersomes with surface-integrated nanoparticles through hierarchical phase separation

Received: 7 August 2024

Accepted: 28 February 2025

Published online: 11 March 2025



Jingxin Shao^{1,7}, Yingtong Luo^{1,7}, Hanglong Wu^{1,2,7}, Jianhong Wang¹, Xuan Zhou³, Süleyman Er³, Shoupeng Cao⁴, Hongyu Sun⁵, H. Hugo Pérez Garza⁵, Hongkui Zheng⁵, Heiner Friedrich^{2,6}, Loai K. E. A. Abdelmohsen¹✉ & Jan C. M. van Hest¹✉

Polymersomes with surface-integrated nanoparticles, in which a smaller sphere is attached to a larger capsule, are typically formed through complex processes like membrane deformation, polymerization, or membrane functionalization. This complexity restricts facile application of this unusual topology, for example in drug delivery or nanomotor science. Our study introduces a robust method for crafting polymersomes with surface-integrated nanoparticles using a hierarchical phase separation approach. By co-assembling block copolymers with aromatic aggregation-induced emission (AIE) moieties as side chains and photothermal-responsive guest molecules (PTM), spontaneous sequential phase separation processes occur that lead to their controlled formation. Polymer-rich liquid droplets form first, followed by internal phase separation of the guest molecules, which determines the formation of asymmetric morphology. This mechanism is elucidated in detail using liquid-phase transmission and cryogenic transmission electron microscopy (LP-TEM and cryo-TEM) and corroborated by theoretical simulations of the interaction forces between the block copolymers and guest molecules. Finally, the application potential of polymersomes with surface-integrated nanoparticles as nanomotors is demonstrated.

Polymersomes are vesicular structures characterized by an aqueous lumen enclosed within a bilayer membrane composed of block copolymers^{1–3}. Over the past few decades, they have emerged as versatile nano-compartments, finding applications in diverse fields such as drug delivery, biocatalysis, cell mimicry, diagnosis, and therapy^{4–7}. The key to their effectiveness in these applications lies in the precise control of their physicochemical properties, encompassing factors like

morphology, surface functionalization, and membrane characteristics^{8–12}. Topological control has thereby become a topic of increased interest in recent years. The construction of polymersomes with non-spherical shape opens up opportunities to study for example these particles in a biomedical context, how they interact with living cells or how topology affects biodistribution. Furthermore, the asymmetric placement of functionality at the polymersomes' surface also

¹Bio-Organic Chemistry, Department of Chemical Engineering and Chemistry, Institute for Complex Molecular Systems (ICMS), Eindhoven University of Technology, Eindhoven, The Netherlands. ²Department of Chemical Engineering and Chemistry, Center for Multiscale Electron Microscopy (CMEM), Eindhoven University of Technology, Eindhoven, The Netherlands. ³DIFFER—Dutch Institute for Fundamental Energy Research, Eindhoven, The Netherlands. ⁴College of Polymer Science and Engineering, Sichuan University, Chengdu, PR China. ⁵DENSsolutions B.V., Delft, The Netherlands. ⁶Laboratory of Physical Chemistry, Department of Chemical Engineering and Chemistry, Eindhoven University of Technology, Eindhoven, The Netherlands. ⁷These authors contributed equally: Jingxin Shao, Yingtong Luo, Hanglong Wu. ✉e-mail: l.k.e.a.abdelmohsen@tue.nl; j.c.m.v.hest@tue.nl

has implications for a range of applications, from drug delivery to nanomotor research.

Polymersomes with asymmetric morphologies can be created either during a direct self-assembly process or through post-formation methods. Polymerization-induced self-assembly (PISA) is arguably the most applied representative of the former process^{13,14}. The latter approach involves different methods, such as membrane deformation by osmotic shock, chemical modification, and chemical/physical metal deposition on the outer membrane, with osmotic pressure being the most extensively utilized strategy^{15–18}. Examples include the transformation of conventional spherical polymersomes into functionally enhanced asymmetric shapes, such as stomatocytes and tubes, Janus nanoparticles, parachute vesicles, and hybrid inorganic-polymer structures^{8,19–24}. Methods for directly achieving shape anisotropy during bottom-up self-assembly of premade building blocks are still limited. This especially holds for more complex topologies such as snowman-shaped capsules with the few reported snowman-shaped capsules based on lipid vesicles rather than polymer vesicles^{25,26}. One of the main reasons is that there is a lack of understanding with respect to the pathways underlying this shape transformation. However, recent progress has been made in the formation of asymmetric polymersomes. Chemotactic synthetic vesicles with asymmetric morphology were created by combining two different copolymers. The formation of asymmetric polymersomes was attributed to two separate domains in the membrane, which laterally segregated²⁷. Recently, there has been a growing recognition of the significance of liquid-liquid phase separation (LLPS) as an intermediate step in the bottom-up amphiphilic self-assembly process. Studies have illustrated the crucial role of transient liquid precursor droplets in controlling the assembly process, where the composition of these droplets determines the morphology of the final assembled structure^{28–32}. For example, adjusting the polymer concentration within liquid droplets can give rise to a wide range of block copolymer assemblies, spanning from polymersomes to bicontinuous spheres^{29,30,33}. This enhanced understanding of liquid-liquid phase separation opens up possibilities for on-demand engineering of polymersome shapes and, more importantly, for introducing functionality into the final assemblies through the precursor droplets. To date, to the best of our knowledge, this strategy has not been realized.

In this study, we present an approach to engineer polymersomes with surface-integrated nanoparticles by precisely controlling hierarchical phase separation during bottom-up self-assembly. Our strategy involves the co-assembly of amphiphilic block copolymers functionalized with aggregation-induced emission (AIE) fluorophores (PEG₄₄-P(AIE)₈) and hydrophobic guests with photothermal-responsiveness (PTM). Upon liquid-liquid phase separation, the precursor phase of the droplet serves as a compartment to accommodate the hydrophobic PTM guest molecules. Subsequently, when hierarchical phase separation is induced in the presence of a water and organic solvent mixture, the guest molecules segregate into an internal phase within the polymer-rich droplets. The sequential co-assembly of the block copolymers and the functional molecules directly leads to the formation of the polymersomes with surface-integrated nanoparticles. Morphological asymmetry of these polymersomes can be finely tuned by adjusting the amount of PTM during the self-assembly process (Fig. 1). To explore the formation mechanism underlying this hierarchical assembly, we employ confocal laser scanning microscopy (CLSM) and liquid-phase transmission electron microscopy (LP-TEM) for real-time observation of the overall formation process and cryogenic transmission electron microscopy (cryo-TEM) for detailed higher-resolution snapshots at specific time point.

This full mechanistic understanding of this process allows the design of polymersomes with unusual topologies and hence additional functions. Since PTM confers not only morphological asymmetry but also photothermal-responsiveness to the polymersomes, the asymmetric structures exhibit the capability to transform into light-propelled nanomotors, with their movement performance manipulated by adjusting the incident laser power.

Results and discussion

Creation and characterization of polymersomes featuring asymmetric morphology (PTM-AIEsomes)

We started this investigation motivated by our interest to construct photothermally responsive polymersomes by encapsulating photothermal-responsive molecules (PTM) as hydrophobic cargo within polymersomes. For this purpose, we employed our recently developed PEG₄₄-P(AIE)₈ block copolymer, which had shown good polymersome formation ability and intrinsic fluorescence. AIE moieties are known to become fluorescent in the assembled state rather

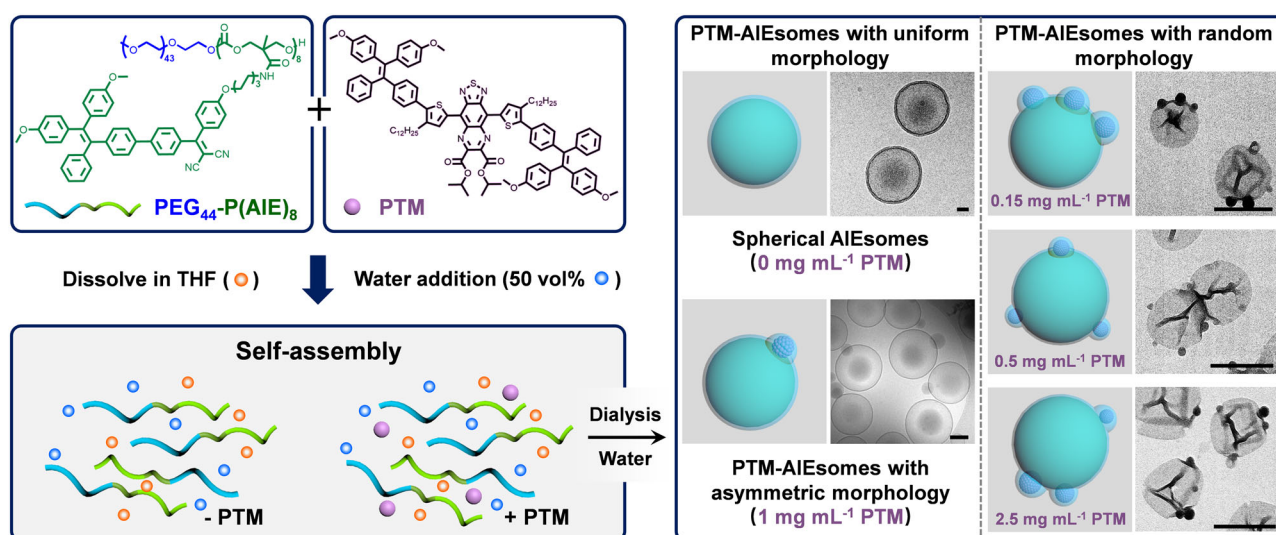


Fig. 1 | Schematic illustrations and TEM images depict PTM-loaded polymersomes (PTM-AIEsomes) exhibiting different morphologies achieved through the modulation of PTM concentration in the self-assembly process. The introduction of 1 mg mL⁻¹ of PTM, in conjunction with 1 mg mL⁻¹ of PEG₄₄-P(AIE)₈,

enables the robust creation of polymersomes with surface-integrated nanoparticles (PTM-AIEsomes) with a consistent structure. Scale bars are 50 nm (0 mg mL⁻¹ PTM), 500 nm (0.15 mg mL⁻¹ PTM), 500 nm (0.5 mg mL⁻¹ PTM), 500 nm (2.5 mg mL⁻¹ PTM), and 200 nm (1 mg mL⁻¹ PTM), respectively.

than in solution. The synthesis of PEG₄₄-P(AIE)₈, composed of poly(ethylene glycol) (PEG) and AIEgenic poly(trimethylene carbonate) (PAIE) segments, was performed according to a previously published protocol³⁴. The second component, PTM, was prepared via a multi-step synthesis process (for details see Supplementary Information, Figs. S1 and S2)³⁵. Initially, an electron-withdrawing acceptor, compound **1**, was synthesized using a reported method^{36–39}. Subsequently, 4-dodecyl-2-thiophene, serving as both a strong electron donor and a π -bridge, was incorporated into the conjugated backbone. Finally, alkoxy-substituted tetraphenylethylene (TPE), which also serves as the second donor, was used to construct D-D'-A-D'-D donor-acceptor type

PTM. The products from each step were characterized using proton nuclear magnetic resonance spectroscopy (¹H NMR) and matrix-assisted laser desorption/ionization time-of-flight mass spectrometry (MALDI-TOF-MS) (Figs. S3–S8). The block copolymers PEG₄₄-P(AIE)₈ and PEG₄₄-P(AIE)₁₄ were also characterized, as shown in Fig. S9. For the generation of polymersomes with photothermal-responsive properties, PEG₄₄-P(AIE)₈ was dissolved with PTM in a THF solution. Milli-Q water was then slowly added (up to 50% vol.) via a syringe pump (Fig. 2a). Subsequently, the resulting cloudy solution underwent dialysis against Milli-Q water for a minimum of 24 h. The hydrodynamic diameter of the as-formed polymersomes (PTM-AIEsomes) was

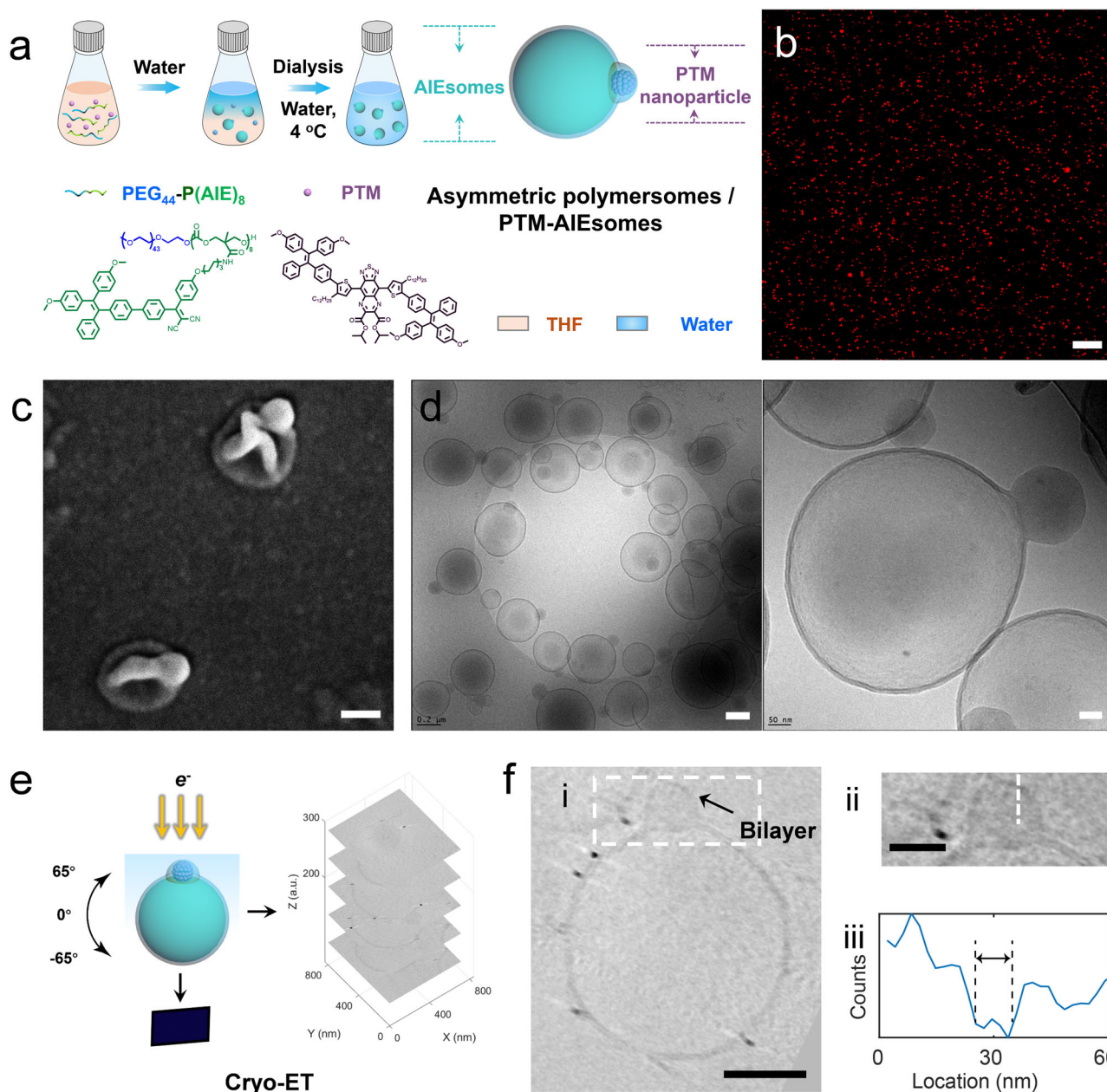


Fig. 2 | Morphological characterization of polymersomes with asymmetric structure (PTM-AIEsomes). **a** Schematic representation of the fabrication process of PTM-AIEsomes through the co-assembly of amphiphilic block copolymers (PEG₄₄-P(AIE)₈) and photothermal molecules (PTM) in the presence of THF and water, followed by dialysis against Milli-Q water. **b** Evaluation of the fluorescence properties of PTM-AIEsomes by confocal laser scanning microscopy (CLSM) with excitation/emission wavelengths of 405 nm/550–650 nm. Scale bar = 20 μ m. **c** Morphological characterization of PTM-AIEsomes using scanning electron

microscopy (SEM). Scale bar = 100 nm. **d** Cryo-TEM image of PTM-AIEsomes (left) and zoomed-in view of an individual PTM-AIEsome (right). Scale bar = 200 nm and 50 nm, respectively. **e** Schematic illustration of cryo-ET. **f** 3D structure analysis of a PTM-AIEsome measured by cryo-ET. (i) Cross-sectional view of a PTM-AIEsome. (ii) Magnified view of the dashed region in (i). (iii) Five-pixel averaged plot profile taken from the dashed line in (ii), showing the bilayer membrane encapsulating the PTM nanoparticle. Scale bar = 200 nm. An additional cryo-ET analysis of PTM-AIEsomes is provided in Fig. S12 of Supplementary Information.

determined by dynamic light scattering (DLS), revealing a size of 373.0 ± 6.5 nm (Fig. S10a), which is in agreement with what would be expected from such a morphological structure⁴⁰. Additionally, one of the distinctive features of polymersomes assembled from PEG₄₄-P(AIE)₈ is their inherent fluorescence. To assess the fluorescence performance of PTM-AIEsomes, confocal laser scanning microscopy (CLSM) was employed (Fig. 2b). A 405 nm laser was utilized to excite the PTM-AIEsomes, and intense fluorescence was detected in the wavelength range of 550–650 nm, according to the optical properties of AIE segment in PEG₄₄-P(AIE)₈. Consequently, the inclusion of PTM into AIEsomes did not impact on their fluorescence properties, affirming that PTM-AIEsomes retain the potential for applications in cell imaging and tracking, akin to pure AIEsomes.

Subsequently, morphological analysis was performed with scanning electron microscopy (SEM) and transmission electron microscopy (TEM). Unexpectedly, the polymersomes exhibited a distinctive trait: a PTM-rich region was connected to the larger polymersomes, creating an asymmetrical morphology (Figs. 2c and S10b). To address potential drying-induced morphological changes in PTM-AIEsomes during SEM and TEM sample preparation, cryogenic transmission electron microscopy (cryo-TEM) analysis was conducted for examination of the native solution structure (Fig. 2d). The asymmetric structure of the PTM-AIEsomes persisted, with each polymersome displaying one PTM nanoparticle. As a control, polymersomes resulting from the self-assembly of pure PEG₄₄-P(AIE)₈ were also prepared (Fig. S10c, d). In contrast to the asymmetric morphology of the PTM-AIEsomes, the pure polymersomes exhibited a spherical morphology. Additionally, cryo-TEM images taken from different orientations of the same PTM-AIEsomes (Fig. S11) allowed us to postulate that the PTM nanoparticle and polymersome form an integral structure, rather than a simple adhesion complex.

To systematically examine the morphology of the PTM-AIEsomes, cryo-electron tomography (cryo-ET) was conducted. Cryo-ET provides 3D structural information of the vesicular membrane of this asymmetric structure and more importantly, the encapsulation site of the PTM nanoparticle. To conduct cryo-ET, a tilt-series was collected to acquire 45 projection images of PTM-AIEsomes before performing 3D volume reconstruction (Fig. 2e)^{34,41,42}. No changes were observed in the sample morphology after acquisition of the tilt-series (Fig. S13). Cross-sections of PTM-AIEsomes from cryo-ET clearly revealed that the PTM nanoparticles were capped by a bilayer membrane (~10 nm) that was slightly deformed at the polymersome/PTM interface (Fig. 2f and Supplementary Movie 1). The intensity line profiles of the bilayer in PTM-AIEsomes have been included as Fig. S12 to enhance visualization of the bilayer membrane and facilitate analysis of its thickness. Furthermore, evidence of the bilayer membrane on PTM nanoparticles can be found in Fig. 14. Interestingly, in a number of cases the bilayer membrane detached from the PTM nanoparticle, leaving the PTM nanoparticle exposed to the aqueous solution, as depicted in Fig. S15. This finding strongly suggests that the formed PTM nanoparticle was initially covered by an additional membrane structure, as a monolayer of PEG₄₄-P(AIE)₈ was necessary to stabilize the hydrophobic PTM nanoparticle in water.

Understanding the molecular features that govern the morphology of PTM-AIEsomes

In order to further understand how this specific morphology of PTM-AIEsomes could be achieved, we systematically adjusted the self-assembly conditions, and varied the molecular features of PTM and PEG₄₄-P(AIE)₈, such as PTM chemical structure (including PTM variants), types of block copolymers (PEG₄₄-P(AIE)₈, PEG₄₄-P(AIE)₁₄, PEG₄₄-*b*-PS₂₀₀, and PEG₄₄-PDLLA₁₂₀) and mixing ratios of the components. Initially, we maintained a constant concentration of PEG₄₄-P(AIE)₈ and co-assembled it with PTM at varying concentrations (Fig. 3a). Subsequent SEM and TEM analyses revealed a uniform and consistent asymmetric

morphology of PTM-AIEsomes exclusively when equal concentrations of PTM and PEG₄₄-P(AIE)₈ were used (third column in Fig. 3a). In contrast, other combinations yielded AIEsomes with multiple PTM nanoparticles integrated in the membrane, along with unencapsulated PTM nanoparticles (first, second, and fourth columns in Fig. 3a). Subsequently, we kept the PTM concentration constant and decreased the concentration of PEG₄₄-P(AIE)₈. Now, the PTM nanoparticles were not incorporated in the membrane but rather formed large aggregates by themselves (Fig. 3b). This indicated that at lower PEG₄₄-P(AIE)₈ concentrations, the majority of AIE-involved block copolymers were utilized to stabilize the PTM particles by forming a monolayer, resulting in a shortage of building blocks for polymersome formation. Reducing the concentration of PEG₄₄-P(AIE)₈ from 0.25 mg mL⁻¹ to 0.125 mg mL⁻¹ resulted in a decrease in the number of polymersomes, thus confirming this hypothesis. Consequently, to achieve homogenous polymersomes with asymmetric morphology, it is essential to ensure that the two building blocks, PTM and PEG₄₄-P(AIE)₈, are used in a 1:1 concentration ratio. Additionally, we maintained this 1:1 ratio but varied the concentrations of PTM and PEG₄₄-P(AIE)₈ simultaneously, testing concentrations of 0.25 mg mL⁻¹, 1.5 mg mL⁻¹, 2 mg mL⁻¹, and 2.5 mg mL⁻¹, respectively. As shown in Figs. S16–S19, homogenous polymersomes with asymmetric morphology, namely one PTM particle associated with one polymersome, were only obtained at a concentration of 0.25 mg mL⁻¹. Based on these investigations, we summarized all experimental conditions and results in Fig. S20 and concluded that the optimal conditions (“sweet spot”) for forming polymersomes with asymmetric topology occur when the concentration ratio of the two building blocks, PTM and PEG₄₄-P(AIE)₈, is 1:1 and each concentration is kept below or equal to 1 mg mL⁻¹ (≤ 1 mg mL⁻¹).

Further exploration involved the examination of the importance of the chemical nature of the amphiphilic block copolymers for the asymmetric topology. For this purpose, three different block copolymers were used which were known to form by themselves well-defined polymersomes: PEG₄₄-P(AIE)₁₄, poly(ethylene glycol)-*block*-polystyrene (PEG₄₄-*b*-PS₂₀₀), and poly(ethylene glycol)-*block*-poly(D,L-lactide) (PEG₄₄-PDLLA₁₂₀). These were subsequently self-assembled with PTM. The same topology was only observed with PEG₄₄-P(AIE)₁₄, akin to the observations with PEG₄₄-P(AIE)₈ (Fig. 4a). In contrast, using PEG₄₄-*b*-PS₂₀₀ and PEG₄₄-PDLLA₁₂₀ predominantly showed free PTM nanoparticles, indicating that these block copolymers primarily stabilized PTM molecules rather than facilitating their inclusion into the polymersome membrane (Fig. S21). Continuing our investigation, we explored the influence of the PTM structure on PTM-AIEsome formation. Keeping the PEG₄₄-P(AIE)₈ component constant at 1 mg mL⁻¹, we co-assembled it with two PTM variants, namely TATQ and TPE-TATQ. Compared to PTM, which has two AIE units, TATQ has no and TPE-TATQ has a single AIE unit (Fig. 4b). However, neither variant exhibited the capacity to form asymmetric polymersomes; instead, polymersomes with uneven sizes were observed. In addition to the PTM variants, we also introduced a hydrophobic dye DiD for co-assembly with PEG₄₄-P(AIE)₈. Again, spherical polymersomes predominated (Fig. 4c). All these hydrophobic guest molecules likely reside within the hydrophobic membrane of the polymersomes, but contrary to PTM don't have an impact on the morphology.

To determine if there is a specific type of intermolecular interaction between the AIE moiety in PEG₄₄-P(AIE)₈ and PTM that plays a pivotal role in PTM-AIEsome formation, we employed density functional theory (DFT) calculations⁴³. The DFT calculations enable a detailed examination of the molecular geometries, energetics, and overall stability of these assemblies, contributing valuable information for the formation of polymersomes with asymmetric morphology^{44–46}. Due to the challenges posed by the large size of the P(AIE)₈ fragment, performing calculations using DFT methods was not practical. Therefore, we employed the AIE monomer as the computational model to facilitate DFT simulations. Our analysis involved a comparison of the

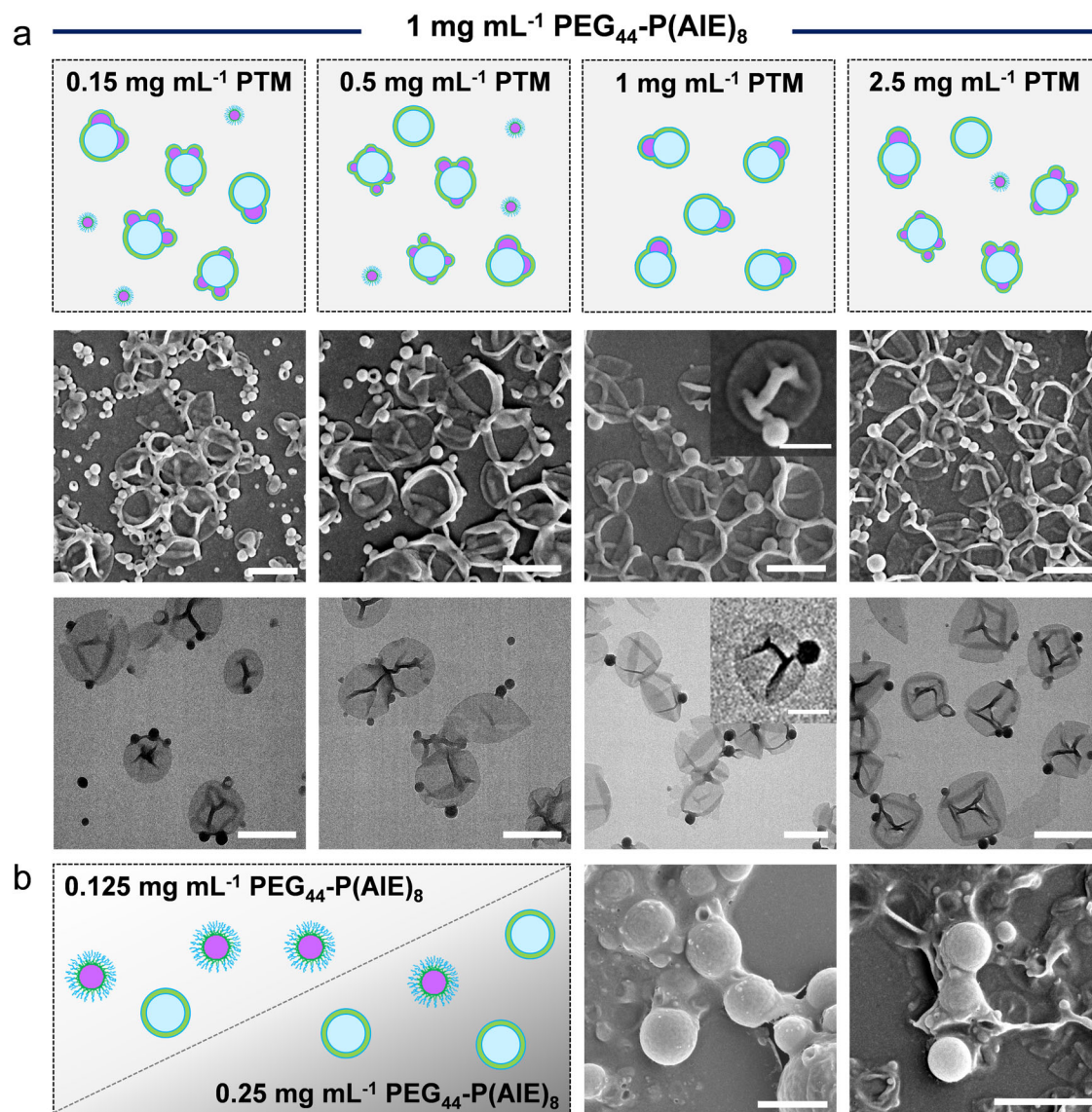


Fig. 3 | Engineering morphological asymmetry in polymersomes by modulating the concentration of PTM and PEG₄₄-P(AIE)₈. **a** Morphological characterization of co-assembled nanoarchitectures was performed as a function of PTM concentration, maintaining a fixed concentration of PEG₄₄-P(AIE)₈ (1 mg mL⁻¹), utilizing SEM (second row) and TEM (third row). Scale bar = 500 nm/Insert = 200 nm. **b** Co-

assembly of PTM (1 mg mL⁻¹) with PEG₄₄-P(AIE)₈ at two different concentrations, 0.125 mg mL⁻¹ (left) and 0.25 mg mL⁻¹ (right), utilizing SEM. Scale bar = 500 nm. The pink color in schematic illustration represents PTM, green and blue color indicate respectively the hydrophobic and hydrophilic domain of amphiphilic block copolymers.

interaction energy between the AIE fragments of amphiphilic block copolymers and PTM, alongside its variants (TPE-TATQ and TATQ). Additionally, we examined the interaction energy between AIE fragments of amphiphilic block copolymers among themselves (Fig. 4d). The interaction energy was calculated using the following equation:

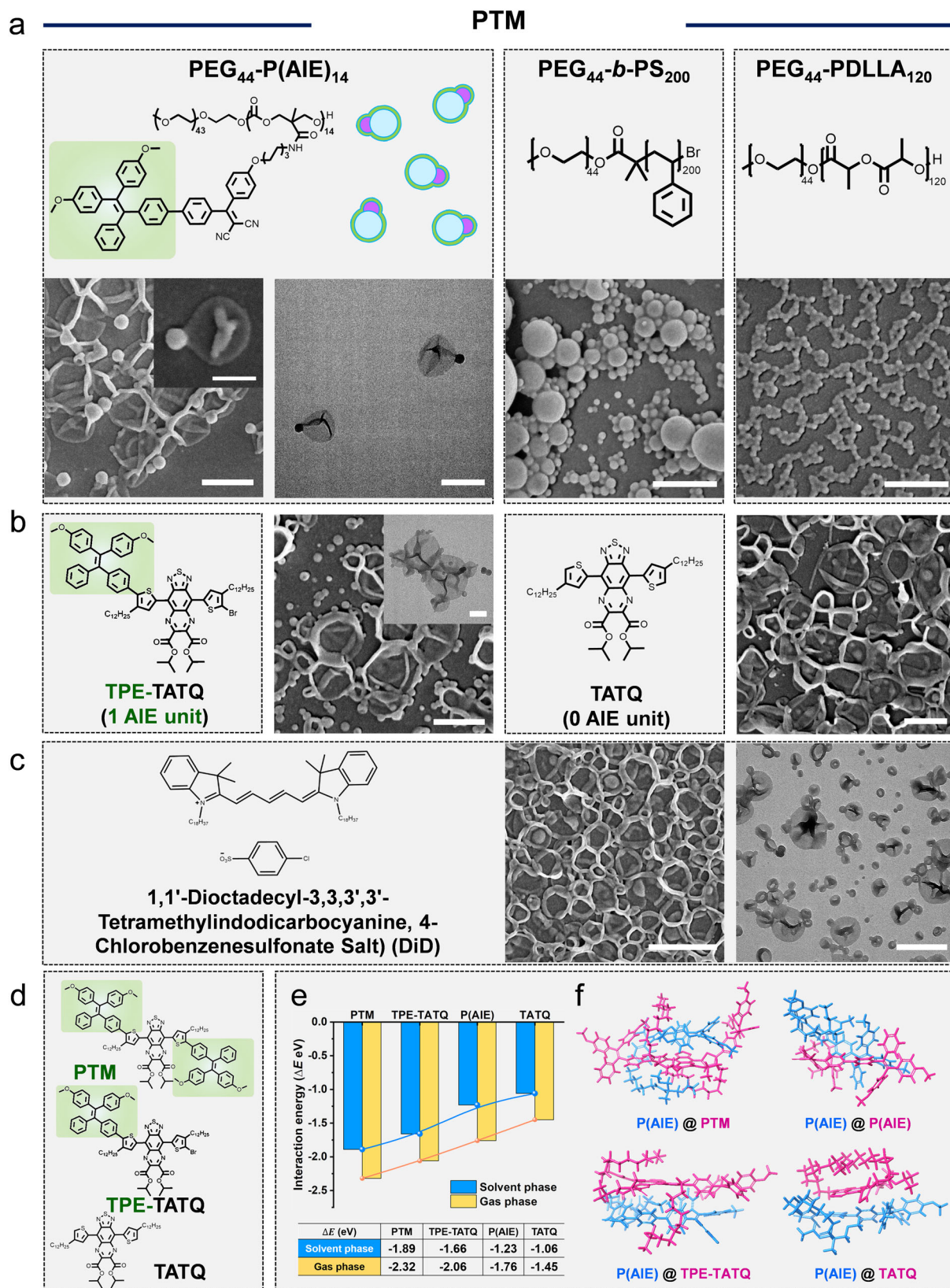
$$\Delta E = E_{\text{Complex}} - E_{\text{AIE}} - E_{\text{Cargo molecule}}$$

where E_{Complex} represents the total energy of the complex formed by a single AIE molecule and a hydrophobic cargo molecule (PTM, TPE-TATQ, or TATQ). E_{AIE} is the total energy of a single AIE molecule, and $E_{\text{Cargo molecule}}$ represents the total energy of the hydrophobic molecule (PTM, TPE-TATQ, or TATQ). Additionally, for interactions between AIE fragments, E_{Complex} represents the total energy of the complex formed by two AIE molecules (P(AIE)), while $E_{\text{Cargo molecule}}$ equals E_{AIE} under these conditions. As depicted in Fig. 4e, a lower ΔE value signifies a more robust interaction between the AIE fragment and the cargo molecule. The results show a progressively enhanced interaction

between the three distinct hydrophobic cargo molecules and the AIE fragment, indicating that as the number of TPE units in the hydrophobic molecule increases, ΔE decreases. The decrease in ΔE is a result of enhanced intermolecular interactions, including van der Waals forces, hydrogen bonding, and Coulombic interactions, stemming from increased wrapping and folding between the molecules, as shown in Fig. 4f. It is suggested that the extension of the TPE fragment in the cargo molecule fosters favorable interactions with the AIE unit. Based on these findings, we propose that strong intermolecular interactions between the AIE moieties of the block copolymers and PTM during the self-assembly process contribute to the formation of polymersomes with surface-integrated nanoparticles, resulting in an asymmetric morphology.

Formation of PTM-AIEsomes through liquid-liquid phase separation

After determining which chemical features play a role in the formation of PTM-AIEsomes with an asymmetric structure, we next monitored



their assembly process by combining liquid phase transmission electron microscopy (LP-TEM) with cryo-TEM. Here, LP-TEM provides useful information on the single-particle history, and cryo-TEM is used to verify the intermediate structures observed in LP-TEM and to provide a closer look at these structures at higher spatial resolution^{47,48}. To mimic the solvent switch process, we performed liquid mixing at

different water/THF mixing rates inside the liquid flow cell (Fig. 5ai)^{29,48,49}. In both slow and fast-mixing experiments, we first filled the liquid cell with block copolymer / PTM dissolved in THF before flowing water into the cell to initiate the self-assembly. To minimize the beam effects on the self-assembly process⁵⁰, a pulsed LP-EM imaging protocol was employed with a low electron flux of $0.2 \text{ e}^- \cdot \text{\AA}^{-2} \cdot \text{s}^{-1}$ (see

Fig. 4 | Morphology characterization using different types of amphiphilic block copolymers and theoretical calculation of interaction energy.

a Nanoarchitectures prepared by co-assembly of PTM (1 mg mL^{-1}) with 1 mg mL^{-1} each of PEG₄₄-P(AIE)₁₄, PEG₄₄-b-PS₂₀₀, and PEG₄₄-PDLLA₁₂₀, respectively. Scale bar = 500 nm. **b** Characterization of polymersomes prepared by co-assembly of PEG₄₄-P(AIE)₈ with two PTM variants (TATQ and TPE-TATQ). Scale bar = 500 nm/Insert = 200 nm. **c** Morphological characterization of DiD load polymersomes by SEM (left) and dry-TEM (right). Scale bar = 1 μm (left) and 500 nm (right).

d Chemical structures of PTM and its variants. In green the AIE moiety is depicted. **e** Interaction energy analysis of the AIE fragments of PEG₄₄-P(AIE)₈ (P(AIE)) with PTM, its variants (TPE-TATQ and TATQ), and P(AIE) in the solvent phase and gas phase via DFT calculations. **f** DFT calculated structures of the AIE fragment of PEG₄₄-P(AIE)₈ interacting with PTM, TPE-TATQ, TATQ, and another AIE fragment (polymer @ polymer). The AIE fragment is highlighted in blue (except in the polymer @ polymer group), while PTM and its variants are depicted in pink.

details of the imaging protocol in “Methods” section). The sample was not exposed to electron beam irradiation between acquisitions. As shown in Fig. 5a, before eventually transforming into PTM-AIEsomes’ asymmetric structure, multiple nanodroplets were formed after 2 h under slow mixing conditions. The PTM nanoparticles formed at the interface between the bilayer of the PEG₄₄-P(AIE)₈ membrane and the THF/water mixture at 20 h, becoming more distinct at 20.5 h. To confirm and better understand the intermediate structure observed by LP-TEM, solvated assemblies at various stages of dialysis were vitrified and analyzed using cryo-TEM (Fig. 5b). Additionally, the pre-assembled polymer solution in 1:1 (v/v) water/THF mixture was also directly “quenched” in water prior to dialysis to investigate the early-stage assembly morphologies (see details in “Methods” section)²². The cryo-TEM data confirmed that the PTM nanoparticles were assembled at the interface of the PEG₄₄-P(AIE)₈-rich droplet, forming a PTM-rich cloud-like structure where micellization of PTM and removal of excessive PEG₄₄-P(AIE)₈ took place. Additionally, freestanding PTM nanoparticles were observed in the solution, as confirmed by both cryo-TEM and LP-EM experiments (Figs. 5b, c, S22 and S23).

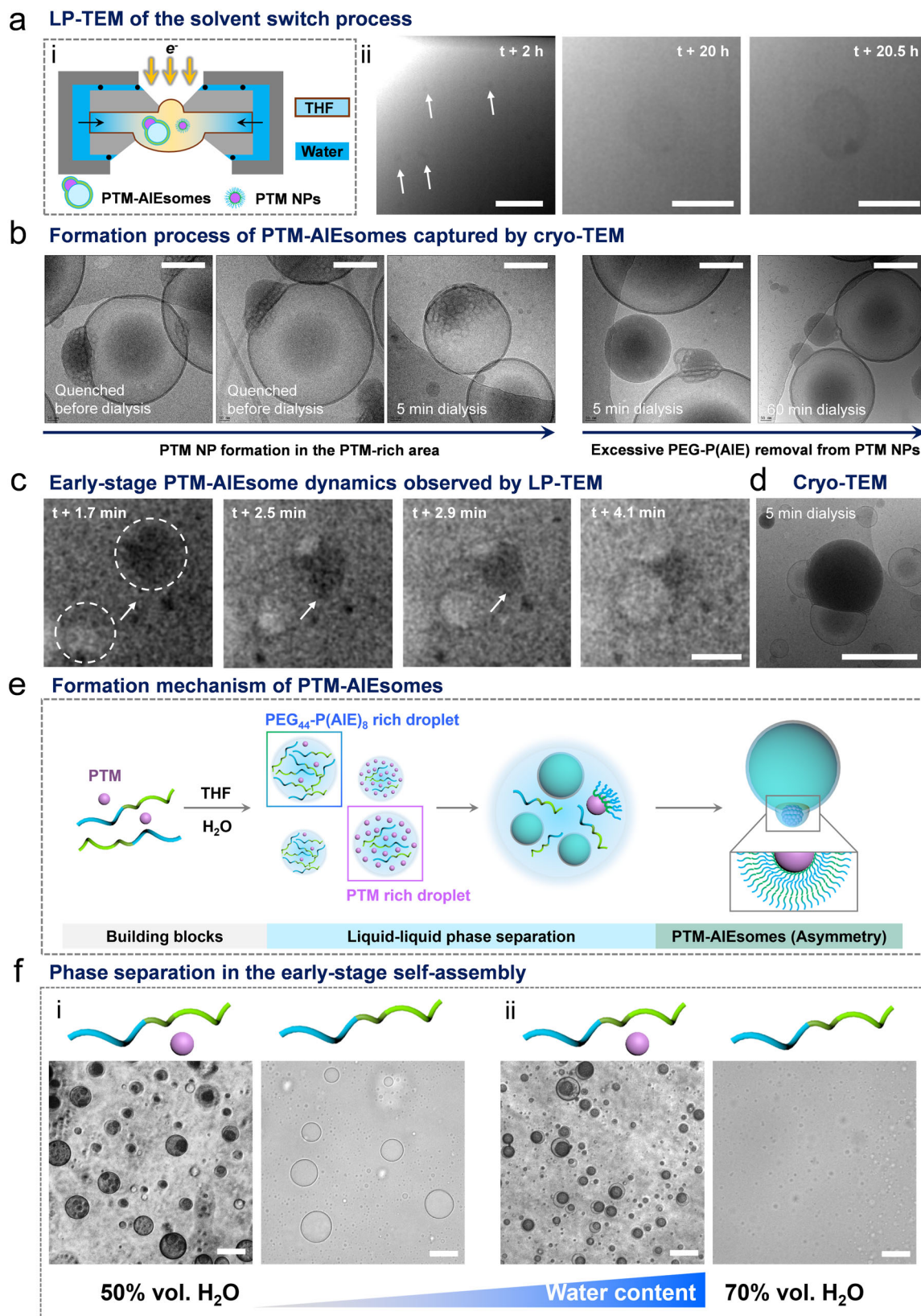
Moreover, the structure of the resulting PTM-AIEsomes is highly dynamic, and fusion events were observed in LP-TEM, which could also be confirmed by cryo-EM (Fig. 5c, d). Based on these observations, we propose that the formation mechanism of PTM-AIEsomes involves liquid-liquid phase separation (Fig. 5e). The formation of PEG₄₄-P(AIE)₈-rich and PTM-rich liquid droplets serves as a precursor in the formation of both PTM-AIEsomes and freestanding PTM nanoparticles, respectively. Notably, PTM molecules exhibit higher hydrophobicity compared to their AIE counterparts. As a result, PTM molecules selectively “attract” PEG₄₄-P(AIE)₈ block copolymers, forming a monolayer protective membrane to stabilize themselves during the solvent switch process. This is supported by the tunability of obtaining pure PTM nanoparticles by adjusting the concentrations of PEG₄₄-P(AIE)₈ to PTM (Fig. 3a, b). To directly observe the onset of phase separation, bright-field images were captured using confocal laser scanning microscopy (CLSM) in the early stage of polymersome formation. As shown in Fig. 5f, phase separation occurred in the presence of both PEG₄₄-P(AIE)₈ and PTM, while only polymer droplets were observed in the absence of cargo molecules (PTM). Interestingly, the size of the droplets decreased with the addition of water, indicating a movement towards equilibrium as the water content increased. The PTM-rich condensates fused together in the multi-phase droplets with the addition of water, which simulated the early stage of the PTM-AIEsomes formation⁵¹. Based on these findings, we propose that polymer-rich liquid droplets initially form, followed by the internal phase separation of PTM guest molecules, thereby determining the morphology of the polymersomes.

Photothermal performance and adaptive motility of PTM-AIEsomes in response to light

Upon laser irradiation, PTM can efficiently convert incident light energy into heat, a characteristic that has been extensively investigated in our prior research³⁵. The maximum absorption peak of PTM falls within the near-infrared window, facilitating effective conversion of incident light energy into heat without fluorescence emission (Fig. S25). Upon co-assembly with PEG₄₄-P(AIE)₈, the absorption peak

of PTM-AIEsomes exhibits a slight red shift compared to pure PTM, yet still remained within the near-infrared window. It is worth mentioning that PTM molecules tend to form J-aggregates when integrated into the polymersomes, as evidenced by the 57 nm red shift in the absorption peak observed between PTM (in THF) and PTM-AIEsomes (in water). Furthermore, we conducted UV-vis spectroscopy measurements during self-assembly of 1 mg mL^{-1} PTM and 1 mg mL^{-1} PEG₄₄-P(AIE)₈ at various time points (0 min, 30 min, 60 min, 90 min, and 120 min) to investigate their kinetics during self-assembly at the molecular level. As shown in Fig. S26, the absorption spectra at 0 min, 30 min, and 60 min exhibited similar features, indicating that PTM remained in a non-aggregated (monomeric) state during this period. However, after 90 min, PTM showed a broadened and red-shifted absorption spectrum, suggesting the formation of J-aggregates between PTM molecules. To assess the photothermal performance of PTM-AIEsomes, we employed an 808 nm laser for irradiation and measured the resulting temperature using a thermometer. Our analysis reveals that PTM-AIEsomes exhibit a robust response to near-infrared irradiation, achieving a temperature change of $34.1 \pm 1.4^\circ\text{C}$ after 10 min of exposure (Fig. 6a). As a control, pure AIEsomes (devoid of PTM) were subjected to identical conditions; however, negligible temperature variations were observed compared to PTM-AIEsomes (Fig. 6b); the maximum temperature attained by AIEsomes after 10 min of irradiation was only $3.9 \pm 0.5^\circ\text{C}$. To quantify the photothermal capability, we further calculated the photothermal conversion efficiency (PCE) of PTM-AIEsomes, which was determined to be 20.7% (Fig. S27). The stability of photothermal heating is crucial for the practical application of PTM-AIEsomes. To assess this, we conducted five cyclic heating-cooling processes and monitored the temperature changes in situ using a thermometer. As illustrated in Fig. 6c, the temperature variations remained consistent within acceptable limits throughout the five cycles. Furthermore, infrared thermographic maps of PTM-AIEsomes (Fig. 6d) provided direct evidence of their photothermal heating capabilities. When combined with their asymmetric morphology, these polymersomes could display motile features^{52–56}. Indeed, PTM-AIEsomes created temperature gradients induced by laser irradiation, resulting in direction motion (Supplementary Movie 2). Notably, the motile behavior of PTM-AIEsomes was easily controlled by adjusting the incident laser’s pathway to steer their direction and by modulating the laser power to manage their velocity (Fig. 6e, f, and Supplementary Movies 3 and 4). Subsequently, we investigated the manipulation of motion by cyclically toggling the incident laser on and off four times. Tracking the corresponding motion trajectories of PTM-AIEsomes and calculating the mean square displacement (MSD) (Fig. 6g) revealed that the motion ceased promptly upon laser deactivation and resumed upon re-illumination. The photothermal stability demonstrated by PTM-AIEsomes in Fig. 6c underpins their controllable movement and instantaneous motion performance.

As control groups, the motion performance of AIEsomes without PTM incorporation was assessed under 808 nm laser irradiation. Only Brownian motion and enhanced diffusion were observed (Fig. S28 and Supplementary Movie 5). These results highlight the potential of PTM-AIEsomes, particularly in biomedicine, owing to their motile properties, biocompatibility, and photothermal responsiveness.



Polymersomes with asymmetric morphology were successfully synthesized through a hierarchical liquid-liquid phase separation assembly process. This asymmetric structure was achieved using AIE fluorophore-functionalized amphiphilic block copolymers PEG₄₄-P(AIE)₈ and photothermal-responsive guest molecules (PTM). Morphological characterization through scanning electron microscopy,

cryogenic transmission electron microscopy, and cryogenic electron tomography, provided direct insights into the asymmetric structure, wherein PTM nanoparticles were integrated into the membrane of the polymer vesicle. The optimal conditions for formation polymersomes with asymmetric topology occur when the PTM and PEG₄₄-P(AIE)₈ are equal (1:1 ratio) and each component is at or below 1 mg mL⁻¹. In situ

Fig. 5 | 3D structure and formation process of PTM-AIEsomes investigated by cryo-TEM and LP-TEM. **a** The formation process of PTM-AIEsomes captured using LP-TEM. (i) Schematic of the liquid cell used to monitor the solvent switch process, mimicking dialysis treatment. (ii) LP-TEM image sequence showing the self-assembly of PTM-AIEsome. Initially, nanodroplets form at 2 h, which eventually transform into PTM-AIEsomes. Scale bar = 2 μm (left), 1 μm (middle), and 1 μm (right). Additional LP-TEM images of nanodroplets are provided in Fig. S24. **b** Cryo-TEM images illustrating the evolution of PTM nanoparticles on AIEsomes. These images were taken from samples directly quenched by adding water before dialysis or at different dialysis times. Scale bar = 200 nm. **c** LP-TEM image sequence revealing the fusion process of early-stage PTM-AIEsomes. Arrows indicate the gradual merging of two PTM-AIEsomes. Scale bar = 500 nm. **d** Cryo-TEM image showing the structure formed from the fusion of two PTM-AIEsomes. Scale bar =

1 μm . **e** Schematic illustration of the proposed formation mechanism of the PTM-AIEsome co-assembly process involving liquid-liquid phase separation. **f** Bright-field images of the early stage of polymersome formation captured by CLSM. (i) Phase separation upon adding 50% vol. H_2O to the assembled solution containing $\text{PEG}_{44}\text{-P(AIE)}_8$ block copolymers and PTM (depicted in the left image). In the absence of PTM, only polymer droplets can be observed (shown in the right image). (ii) With the addition of 70% vol. H_2O , phase separation occurs in the mixed solution of $\text{PEG}_{44}\text{-P(AIE)}_8$ and PTM (shown in the left image), while no phase separation is observed in the pure $\text{PEG}_{44}\text{-P(AIE)}_8$ solution (depicted in the right image). Scale bar = 20 μm . The initial polymer concentration for cryo-TEM, LP-TEM, and CLSM is 1 mg mL^{-1} PTM, and 1 mg mL^{-1} $\text{PEG}_{44}\text{-P(AIE)}_8$ dissolved in THF solution. Further details can be found in the “Methods” section.

observation of the self-assembly process using liquid-phase transmission electron microscopy confirmed the formation mechanism, involving a hierarchical liquid-liquid phase separation process of PTM molecules and the block copolymers. Coexisting $\text{PEG}_{44}\text{-P(AIE)}_8$ rich droplets and PTM-rich droplets acted as precursors for both PTM-AIEsomes and freestanding PTM nanoparticles. A monolayer protective membrane was formed on the PTM particles due to their higher hydrophobicity, stabilizing them before fusion with the polymersomes to form PTM-AIEsomes. With a photothermal conversion efficiency of 20.7% (using an 808 nm laser), PTM-AIEsomes can function as light-driven nanomotors with controllable motion by adjusting the laser's path and power. Unlike most previous photothermal nanomotors made using gold-based materials (e.g., gold nanoparticles or gold layer coated particles), PTM-AIEsomes are fully organic and fundamentally different. Their asymmetric morphology is programmed during self-assembly rather than modified afterward. Furthermore, we introduced photothermal-responsive cargos, enhancing both functionality and responsiveness in these polymersomes. These advancements make significant progress in developing fully organic photothermal nanomotors. Additionally, a comprehensive understanding of the liquid-liquid phase separation process, achieved through advanced characterization techniques, facilitates the development of polymersomes with asymmetric morphology and multiple functions.

Methods

Synthetic procedures

Compound TPE-Cl was prepared according to previously published protocols with some modifications⁵⁷. Briefly, bis(4-methoxyphenyl) methanone (9.73 g, 40.0 mmol), 4-chloro-benzophenone (10.4 g, 48.0 mmol), and Zn powder (13 g, 200 mmol) were dissolved in dry THF (500 mL) which was pre-cooled in an ice bath under argon atmosphere. Titanium tetrachloride (TiCl_4 , 17.6 mL, 160 mmol) was thereafter added slowly to the above-mentioned mixture under stirring, followed by heating to 80 $^{\circ}\text{C}$. After reaction for 24 h, the reaction mixture was cooled to room temperature before quenching with 250 mL 10% K_2CO_3 (aqueous solution). Then, the reaction mixture was filtered to remove the insoluble materials and washed with CH_2Cl_2 solution. The organic layer was dried with anhydrous MgSO_4 and filtered, after which CH_2Cl_2 was removed via evaporation. Next, the residue was purified by silica gel chromatography with a mixture of hexane and CH_2Cl_2 ($V_1:V_2 = 5:1$) as the eluent. The obtained compound TPE-Cl was a light yellow solid (9.42 g, 46% yield). ^1H NMR (400 MHz, CDCl_3) δ (ppm): 7.14–7.04 (m, 5H), 7.01–6.98 (m, 2H), 6.95–6.90 (m, 6H), 6.67–6.61 (m, 4H), 3.76 (d, $J = 12$ Hz, 6H).

Compound TPE-PIN was synthesized according to previously reported protocols with some modifications^{34,35}. Briefly, TPE-Cl (426 mg, 1 mmol), bis(pinacolato)diboron (B_2Pin_2) (1.53 g, 6 mmol), X-Phos Pd G2 precatalyst (40 mg, 0.05 mmol), and potassium acetate (KOAc) (590 mg, 6 mmol) were dissolved in anhydrous 1,4-dioxane (5 mL) under nitrogen atmosphere. Then, the mixture was heated to 90 $^{\circ}\text{C}$ and stirred for 24 h. After cooling to room temperature, the

reaction mixture was poured into 50 mL water and extracted with EtOAc (50 mL). The combined organic phase was dried by anhydrous MgSO_4 , followed by filtering, and concentrating under vacuum. The crude product was used for the next step for the synthesis of PTM without further purification. ^1H NMR (400 MHz, CDCl_3) δ (ppm): 7.55 (d, $J = 8$ Hz, 2H), 7.10–6.98 (m, 7H), 6.94–6.92 (m, 4H), 6.63 (d, $J = 8$ Hz, 4H), 3.73 (d, $J = 4$ Hz, 6H), 1.32 (s, 12H).

Compound **1** was synthesized according to previously reported procedures³⁷. 4,7-Dibromobenzo[c][1,2,5]thiadiazole-5,6-diamine (1.50 g, 4.63 mmol) and 1,4-Bis(1-methylethyl) 2,3-dioxobutanoate (2.56 g, 11.11 mmol) were dissolved in acetic acid (40 mL) under a nitrogen atmosphere. The resulting mixture was heated to 100 $^{\circ}\text{C}$ and stirred for 24 h. After cooling to room temperature, the reaction mixture was poured into 100 mL water and extracted with dichloromethane three times. The combined organic phase was dried by anhydrous magnesium sulfate, filtered and concentrated under vacuum. The residue was purified by silica gel chromatograph with petroleum ether/dichloromethane ($V_1:V_2 = 5:1$) as the eluent. The product was an orange crystal (1.08 g, yield: 45%). ^1H NMR (400 MHz, CDCl_3) δ (ppm) = 5.45–5.40 (m, 2H), 1.50–1.49 (d, 12H).

Compound **2**: Compound **1** (518 mg, 1 mmol), $\text{Pd}_2(\text{dba})_3$ (73 mg, 0.08 mmol), $\text{P}(\text{o-tol})_3$ (73 mg, 0.24 mmol), and stannane, (4-dodecyl-2-thienyl)trimethyl (1.04 g, 2.5 mmol) were dissolved in 5 mL chlorobenzene under nitrogen atmosphere. Then, the mixture was heated to 110 $^{\circ}\text{C}$ and reacted for 48 h under stirring. After cooling to room temperature, the reaction mixture was poured into 30 mL water and extracted with dichloromethane three times. The combined organic phases were dried by anhydrous MgSO_4 , followed by filtering and concentrating under vacuum. The product was purified by silica gel chromatography with hexane/dichloromethane ($V_1:V_2 = 3:1$) as the eluent. The product was a dark blue solid (620 mg, 70% yield). ^1H NMR (400 MHz, CDCl_3) δ (ppm) = 8.80 (s, 2H), 7.34 (s, 2H), 5.50–5.42 (m, 2H), 2.75–2.71 (m, 4H), 1.78–1.69 (m, 4H), 1.53 (d, 12H), 1.44–1.26 (m, 36H), 0.89–0.86 (m, 6H). MALDI TOF-MS: m/z calculated for $[\text{M}]^+$ $\text{C}_{48}\text{H}_{68}\text{N}_4\text{O}_4\text{S}_3$, 860.44, found 860.43. ^{13}C NMR (100 MHz, CDCl_3) δ (ppm): 163.66, 152.21, 143.35, 142.97, 135.42, 133.98, 129.19, 122.49, 71.52, 70.03, 33.22, 31.92, 30.65, 29.71, 28.46, 23.85, 22.54, 21.29, 20.02, 16.01, 14.76, 13.53, 12.29.

Compound **3**: Compound **2** (500 mg, 0.58 mmol) was dissolved in a mixture of CHCl_3 (12 mL) and acetic acid (6 mL) under argon atmosphere, followed by adding NBS (206 mg, 1.16 mmol) slowly over the course of 30 min with the exclusion of light. The resulting mixture was stirred for 12 h at room temperature. Next, the reaction mixture was poured into 30 mL water and extracted with dichloromethane three times. The combined organic phases were dried with anhydrous MgSO_4 , filtered, and concentrated under vacuum. The as-prepared product was then purified by silica gel chromatography with hexane/dichloromethane ($V_1:V_2 = 3:1$) as the eluent. 472 mg compound **3** (light green solid) was obtained (80% yield). ^1H NMR (400 MHz, CDCl_3) δ (ppm) = 8.68 (s, 2H), 5.53–5.44 (m, 2H), 2.62–2.58 (m, 4H), 1.67–1.64 (m, 4H), 1.59 (d, 12H), 1.37–1.26 (m, 36H), 0.89–0.85 (m, 6H). MALDI TOF-

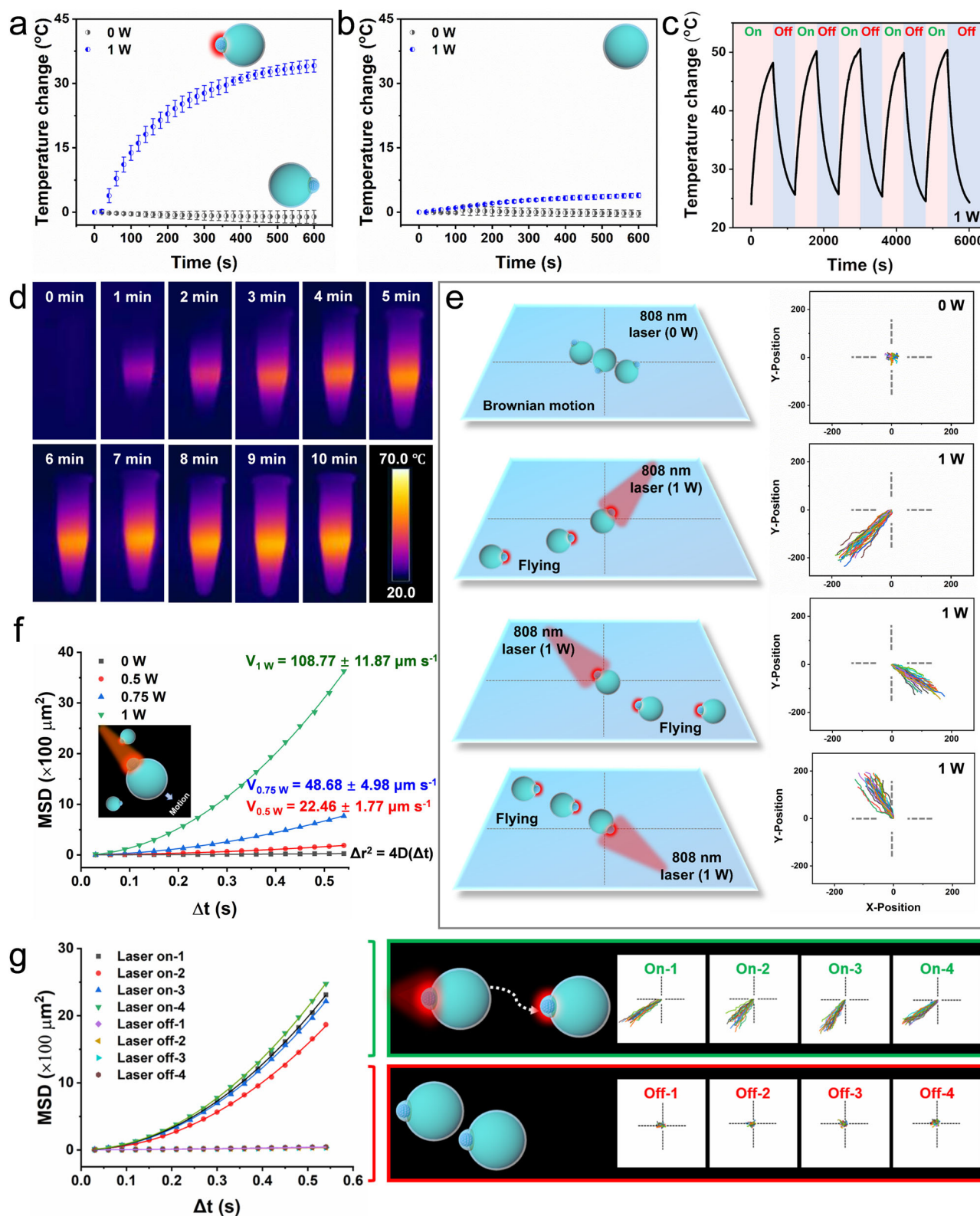


Fig. 6 | Photothermal performance and motile behavior of PTM-AIEsomes.

a Temperature curves of PTM-AIEsomes (1 mg mL⁻¹) in Milli-Q water induced by near-infrared laser (NIR, 808 nm) irradiation at different power levels (0 W and 1 W). **b** Temperature curves of spherical AIEsomes (without PTM encapsulation) in Milli-Q water (1 mg mL⁻¹) upon 808 nm laser irradiation at different power levels (0 W and 1 W). **c** Temperature variations of PTM-AIEsomes under periodic 808 nm laser irradiation (1 W). **d** Infrared thermographic maps of PTM-AIEsomes in aqueous solution within a tube under 808 nm laser irradiation (1 W). **e** Tracked motion

trajectories of PTM-AIEsomes with and without 808 nm laser irradiation, illustrating manipulation in motion direction by changing the incident laser pathway. **f** Mean square displacement (MSD) and velocity of PTM-AIEsomes under laser irradiation as a function of output laser power. The velocity of each group was calculated from $\text{MSD} = (4D)\Delta t + (v^2)(\Delta t^2)$. **g** Start-Stop periodic motion of PTM-AIEsomes by alternately turning on and off the incident laser (808 nm, 1 W). Motion characterization via MSD (left) and corresponding motion trajectories (right).

MS: m/z calculated for $[M]^+ C_{48}H_{66}Br_2N_4O_4S_3$, 1018.25, found 1018.25. ^{13}C NMR (100 MHz, $CDCl_3$) δ (ppm): 163.04, 150.95, 141.84, 141.55, 135.17, 133.43, 132.56, 120.25, 71.61, 70.00, 33.23, 31.97, 31.67, 31.03, 29.80, 28.53, 24.01, 22.84, 21.44, 20.23, 16.03, 14.75, 13.52, 12.32.

Compound 4: Compound **3** (300 mg, 0.3 mmol), TPE-PIN (78 mg, 0.15 mmol), potassium carbonate (324 mg, 2.36 mmol), and $Pd(PPh_3)_4$ (5% catalytic equivalent) were dissolved in a solution of THF (9 mL) and water (3 mL) under argon atmosphere. The reaction mixture was heated to 60 °C and reacted for 12 h under stirring. The product was extracted with dichloromethane and washed with water after cooling to room temperature. The combined organic phase was dried by anhydrous $MgSO_4$, filtered and concentrated under vacuum. The residue was purified by silica gel chromatography with hexane/dichloromethane ($V_1:V_2 = 1:1$) as the eluent. The obtained product was a dark green solid (60 mg, 30% yield). 1H NMR (400 MHz, $CDCl_3$): δ (ppm) = 8.99 (s, 1H), 8.88 (s, 1H), 7.34 (d, 2H), 7.17–7.07 (m, 7H), 7.01–6.95 (m, 4H), 6.68–6.64 (m, 4H), 5.46–5.38 (m, 2H), 3.75 (s, 6H), 2.80–2.74 (m, 4H), 1.77–1.66 (m, 4H), 1.58 (d, 12H), 1.37–1.25 (m, 36H), 0.89–0.85 (m, 6H). MALDI TOF-MS: m/z calculated for $[M]^+ C_{76}H_{89}BrN_4O_6S_3$, 1330.51, found 1330.59. ^{13}C NMR (100 MHz, $CDCl_3$) δ (ppm): 163.58, 163.34, 158.25, 151.87, 151.39, 142.18, 136.42, 136.35, 135.41, 134.02, 133.42, 132.34, 131.90, 130.81, 128.66, 120.05, 114.01, 71.61, 71.34, 70.12, 69.90, 55.82, 54.37, 32.00, 31.05, 29.82, 29.49, 28.57, 28.27, 24.02, 22.85, 22.77, 21.55, 21.38, 14.15, 13.61.

Compound 5: Compound **3** (300 mg, 0.3 mmol), TPE-PIN (393 mg, 0.76 mmol), potassium carbonate (324 mg, 2.36 mmol), and $Pd(PPh_3)_4$ (5% catalytic equivalent) were dissolved in a solution containing 9 mL THF and 3 mL water under argon atmosphere. The reaction mixture was heated to 60 °C and stirred for 12 h. After cooling to room temperature, the reaction mixture was extracted with dichloromethane and washed with water. The combined organic phase was dried using anhydrous $MgSO_4$, followed by filtering and concentrating under vacuum. The residue was purified by silica gel chromatography using hexane/dichloromethane ($V_1:V_2 = 1:1$) as the eluent. The obtained compound **5** was a dark green solid (295 mg, 60% yield). 1H NMR (400 MHz, $CDCl_3$): δ (ppm) = 8.98 (s, 2H), 7.35 (d, 4H), 7.11–7.08 (m, 10H), 7.01–6.95 (m, 10H), 6.68–6.64 (m, 10H), 5.46–5.38 (m, 2H), 3.75 (s, 12H), 2.80–2.74 (m, 4H), 1.75–1.67 (m, 4H), 1.45 (d, 12H), 1.37–1.25 (m, 36H), 0.89–0.85 (m, 6H). MALDI TOF-MS: m/z calculated for $[M]^+ C_{104}H_{112}N_4O_8S_3$, 1641.76, found 1641.76. ^{13}C NMR (100 MHz, $CDCl_3$) δ (ppm): 163.79, 158.20, 152.34, 142.79, 140.62, 138.74, 136.43, 134.10, 133.55, 132.34, 130.75, 129.13, 128.61, 127.49, 127.03, 125.45, 121.89, 113.94, 112.31, 71.45, 69.97, 57.26, 55.84, 54.37, 52.94, 30.98, 29.73, 28.47, 22.53, 21.25, 14.78, 13.55.

Preparation of biodegradable polymersomes with aggregation-induced emission (AIEsomes)

Amphiphilic block-co-polymers PEG-P(AIE)₈ and PEG-P(AIE)₁₄ were synthesized according to the previously reported methodology^{34,42,58}. Specific protocols were summarized as follows.

PEG₄₄-P(AIE)₈: Freeze dried PEG₄₄-PTMCP₈ (92 mg, 0.02 mmol) was dissolved in 1 mL of dry THF and cooled in an ice bath. A 0.5 mL THF solution containing AIE-NH₂ (180 mg, 0.18 mmol, relative to the pentafluorophenyl ester) and trimethylamine (TEA, 34 μ L, 0.18 mmol, relative to the pentafluorophenyl ester) were then dropwise added. Afterward, the ice bath was removed, and the mixture was stirred for an additional 90 min. The reaction progress was monitored by 1H NMR and ^{19}F NMR. Once the pentafluorophenyl ester was fully converted, the reaction solution was precipitated into diethyl ether three times. The resulting yellow solid was isolated and freeze dried to obtain PEG₄₄-P(AIE)₈. The copolymer composition was calculated by using the proton signals of PEG (3.61–3.68 ppm), the terminal methyl unit (singlet at 3.38 ppm), TMCAIE CH₂ (m, 3.70–3.76 ppm) and TMCAIE CH₂ (m, 4.22–4.32 ppm), and TMCAIE CH₂ (m, 6.60–6.66 ppm).

PEG₄₄-P(AIE)₁₄: Freeze dried PEG₄₄-PTMCP₁₄ (131 mg, 0.02 mmol) was dissolved in 1 mL of dry THF and cooled in an ice bath. Next, a

0.5 mL THF solution containing AIE-NH₂ (314 mg, 0.32 mmol, relative to the pentafluorophenyl ester) and trimethylamine (TEA, 60 μ L, 0.32 mmol, relative to the pentafluorophenyl ester) were dropwise added. The ice bath was removed, and the mixture was stirred for an additional 90 min. The reaction progress was monitored by 1H NMR and ^{19}F NMR. After the complete conversion of pentafluorophenyl ester, the reaction solution was precipitated into diethyl ether three times. Then the yellow solid was isolated and freeze dried to obtain PEG₄₄-P(AIE)₁₄.

For the self-assembly into polymersomes (AIEsomes), PEG₄₄-P(AIE)₈ block copolymer was dissolved in 0.5 mL pure THF solution (2 mg mL⁻¹) in a glass vial with a magnetic stirring bar. After stirring for 30 min, 0.5 mL of ultrapure Milli-Q water was added via a syringe pump (Chemyx, Inc., Fusion 100, KR Analytical Limited, Stafford, TX, USA) with a speed of 0.25 mL h⁻¹. The resulting cloudy solution was transferred into a 2 mL cm⁻¹ pre-hydrated dialysis bag (MWCO 12,000–14,000, Spectra/Pro®, Rancho Dominguez, CA, USA) for dialysis against Milli-Q water at 4 °C with a water change after 1 h, followed by dialyzing for at least 24 h. The physicochemical properties of AIEsomes were characterized by scanning electron microscopy (SEM), transmission electron microscopy (TEM), and cryogenic TEM (cryo-TEM).

Formation of asymmetric polymersomes (PTM-AIEsomes) by co-assembly of block copolymers PEG₄₄-P(AIE)_{8/14} and PTM

PTM cargo (0.15 mg, 0.5 mg, 1 mg, and 2.5 mg) was dissolved in 0.5 mL PEG₄₄-P(AIE)₈ polymer solution (THF, 2 mg mL⁻¹), respectively. After stirring for 30 min, 0.5 mL of ultrapure Milli-Q water was added through a syringe pump (0.25 mL h⁻¹). The obtained cloudy green solution (1 mL) was transferred into a 2 mL cm⁻¹ pre-hydrated dialysis bag (MWCO 12,000–14,000) and dialyzed against 1 L of Milli-Q water at 4 °C, with the water being changed after 1 h. It is important to mention that the dialysis solution (Milli-Q water) was changed only once. The whole dialysis procedure was at least 24 h. During dialysis, stirring was performed using a stirring plate (IKA) at a speed of 300 rpm. The morphological characterization of asymmetric polymersomes was conducted by SEM, TEM, cryo-TEM, dynamic light scattering (DLS), cryo-electron tomography (cryo-ET). PEG₄₄-P(AIE)₁₄ was used as control group, and self-assembled into PTM-AIEsomes following the above-mentioned procedure. By following the above-mentioned procedure, polymersomes with surface-integrated nanoparticles, specifically PTM-AIEsomes, can be reproduced.

Preparation of PTM-loaded polymersomes using PEG₄₄-*b*-PS₂₀₀ and PEG₄₄-PDLLA₁₂₀

PTM cargo (1 mg mL⁻¹) was co-assembled with PEG₄₄-*b*-PS₂₀₀ (1 mg mL⁻¹) in dioxane/THF mixture (4/1, v/v), followed by stirring for 30 min. After adding 0.5 mL ultrapure Milli-Q water via a syringe pump (1 mL h⁻¹), the cloudy solution was transferred into a 2 mL cm⁻¹ pre-hydrated dialysis bag (MWCO 12,000–14,000) and dialyzed against 1 L of Milli-Q water at 4 °C, with the water being changed after 1 h and continued dialysis for at least 24 h. It is important to mention that stirring was performed during dialysis using a stirring plate (IKA) at a speed of 300 rpm. When changing the block copolymer from PEG₄₄-*b*-PS₂₀₀ to PEG₄₄-PDLLA₁₂₀, all the procedures were the same, besides that PTM and PEG₄₄-PDLLA₁₂₀ were dissolved in a THF/dioxane mixture (4/1, v/v). The obtained samples were characterized using SEM.

Co-assembly of different hydrophobic cargos with block copolymer PEG₄₄-P(AIE)₈

As control groups, compound **2** (TATQ, 1 mg mL⁻¹), compound **4** (TPE-TATQ, 1 mg mL⁻¹), and the hydrophobic dye DiD were co-assembled with PEG₄₄-P(AIE)₈ (1:1, w/w) according to the same procedures as

described for PTM-AIEsomes. The physicochemical properties of the control groups were evaluated by SEM and TEM.

Time-resolved cryo-TEM on the formation process of PTM-AIEsomes

The formation process of PTM-AIEsomes during dialysis was monitored by time-resolved cryo-TEM. Aliquots of PTM-AIEsomes were taken from the dialysis bag at different times and rapidly vitrified in liquid ethane. To prevent THF evaporation, particularly for samples in the first 10 min of dialysis, an atmosphere containing THF vapor was created by placing filter papers fully absorbed with THF in the vitrobot chamber before vitrification. To gain a better understanding of the morphology of PTM-AIEsomes during early-stage self-assembly, the cloudy polymer solution in a water/THF mixture (1:1, v/v) was directly quenched in water (200 μL polymer solution + 1 mL water) before being vitrified in liquid ethane. It is worth noting that the initial polymer concentration in THF prior to co-assembly is 1 mg mL⁻¹ PTM and 1 mg mL⁻¹ PEG₄₄-P(AIE)₈ dissolved in THF.

Cryo-electron tomography (cryo-ET)

The acquisition of cryo-ET tilt-series was conducted using Inspect 3D software from Thermo Fisher Scientific. The alignment of the tilt-series (Fig. S13a) and tomographic reconstruction (Fig. S13b) were performed using the simultaneous iterative reconstruction technique (SIRT) in IMOD⁵⁹, with 20 iterations. The parameters used in the cryo-ET experiments are shown below:

Angular sampling : -65° to 65° at 4° increments; Pixel size : 0.62 nm.

Magnification : 15000 \times ; Defocus : $-4\mu\text{m}$;

Total image number : 33; Electron dose : $\sim 4.9\text{ e}^-/\text{\AA}^2/\text{frame}$

The detrimental effects of electron beam exposure on polymer-some morphology at this total dose was checked after tilt-series acquisition. No changes were observed in the sample morphology after the tilt-series (Fig. S13c).

Liquid phase transmission electron microscopy (LP-TEM)

To monitor the self-assembly process of PTM-AIEsomes, we conducted a series of LP-TEM experiments to replicate the solvent switch process inside the liquid cell. Initially, the liquid cell was filled with a mixture of polymer solution (1 mg mL⁻¹ PTM + 1 mg mL⁻¹ PEG₄₄-P(AIE)₈ dissolved in THF), followed by the flow of water to initiate the self-assembly. Two types of liquid flow cells were used to control the mixing rates of water and polymers in THF. The first type, denoted as the bypass liquid cell, allowed for gradually increasing the water concentration in the viewing window area through water diffusion. The second type, denoted as the direct-flow liquid cell, rapidly replaced the organic solvent with water^{48,49}.

Different polymer sample loading methods were used for the two types of liquid cell experiments. The bypass LP-TEM experiments were performed in the Ocean liquid flow holder. The polymer sample was loaded (2 μL) by drop casting and the liquid cell assembly was carried out in a custom environmental chamber with the presence of THF vapor. The flow of water into the liquid cell was initiated immediately after the assembly of the liquid cell. In the direct-flow LP-TEM experiments, the polymer solution was manually injected into the Stream liquid cell holder using a THF-compatible syringe (1 mL). Subsequently, the polymer solution was purged from the lines of the liquid cell holder within THF-saturated vapor until no solution came out from the exit line. Then, water was introduced into the holder to initiate self-assembly by using a pressure pump with a pressure ranging from 300 mbar to 1.5 bar.

During the fast-mixing experiments, it was found that the on-chip liquid flow channel was prone to clogging due to the rapid

accumulation of PTM nanoparticles at the inlet of the chip. This is likely due to the higher hydrophobicity of PTM compared to AIE counterparts, resulting in the preferential assembly of PTM into micelle-like nanoparticles at the water/THF interface. The clogging of the flow channel can cause the formation of PTM-AIEsomes to cease as water flow stops. We noted that increasing the flow pressure can unclog the holder, allowing for the self-assembly of PTM-AIEsomes to continue. During unclogging, a significant amount of PTM nanoparticles were observed to be flushed into the viewing area (Fig. S22).

The formation process of PTM-AIEsomes was monitored using a pulsed LP-TEM imaging protocol with a controlled electron flux of $\sim 0.2\text{ e}^-/\text{\AA}^2\text{ s}^{-1}$ ⁴⁶. Images were recorded at 5000 \times magnification every 5–10 min. It is important to note that the frequency of image acquisition varied depending on the kinetics of the reaction. Some images were taken every few tens of seconds and others every few hours. The electron beam was blanked between image acquisition. The cumulative dose applied was typically less than $5\text{ e}^-/\text{\AA}^2$ for the direct-flow liquid cell experiments and up to $15\text{ e}^-/\text{\AA}^2$ for the experiments in the bypass system. Given the slow reaction kinetics (typically $\sim 20\text{ h}$) and the thick liquid layer (1 μm) present in the bypass cell, we mainly focused on the first 2 h after the flow of water to investigate the early-stage self-assembly behaviors, with up to a cumulative dose of $5\text{ e}^-/\text{\AA}^2$ applied. The beam was then blanked at various locations for different periods of time to investigate the evolution of assemblies over time.

Evaluation of fluorescence properties of spherical AIEsomes and PTM-AIEsomes

The UV-absorbance and fluorescence spectrum of PTM and PTM-AIEsomes were characterized using UV-vis spectrophotometry and fluorescence spectrophotometry. To characterize PTM, the solvent used to dissolve Compound **5** were DCM, DMF, and THF, respectively. For PTM-AIEsomes, the solvent was Milli-Q water.

Computational methods

All the calculations in the current study were implemented using the Schrödinger Materials Science Suite (SMSS)⁶⁰. The initial geometry was constructed using the Maestro editor. The OPLS4 force field (FF) was employed to perform the conformational search for the AIE unit, three compounds (PTM, TPE-TATQ, and TATQ), and the complex models of the AIE unit and compounds⁶¹. Besides, molecular dynamics (MD) simulations were applied to generate the structural conformers for the complex models. The generated structural conformers, including the lowest-energy conformers of AIE, three compounds and their complex models from FF, as well as the structural framework of their complex models after 20-ns and 100-ns MD simulations, were optimized in the gas phase. The solvent-phase single point energy (SPE) was then calculated on each optimized geometry. The MacroModel module, and Desmond package, as implemented in SMSS, were employed for FF and MD calculations, respectively^{62,63}. The OPLS4-FF and the canonical (NVT) ensemble class were applied in MD simulations⁶⁴. The Jaguar program was used for all the density functional theory (DFT) calculations⁶⁵. The B3LYP-D3 functional and LACVP⁺⁺ basis set with polarization and diffuse functions were employed for DFT calculations^{66,67}. The convergence criteria for the changes in energy and Root Mean Square (RMS) density matrix were 5×10^{-5} and 5×10^{-6} Hartree, respectively. The grid density and accuracy level were set “Medium” and “Quick” for DFT optimizations, and “Fine” and “Accurate” for DFT SPE calculations. The standard Poisson-Boltzmann Formalism (PBF) was employed as solvation model and the water was selected as solvent⁶⁸.

Photothermal conversion efficiency (PCE)

The photothermal conversion efficiency (PCE) of PTM-AIEsomes under 808 nm laser irradiation was calculated according to published protocols^{35,69}. Briefly, the photothermal heating of an aqueous solution

of PTM-AIEsomes was measured through a thermometer under 808 nm laser irradiation. Then, the PCE was calculated using the following Eq. (1):

$$\eta = \frac{hA(T_{\max} - T_{\text{surr}}) - Q_{\text{dis}}}{I(1 - 10^{-A_{808}/808})} \quad (1)$$

Here, η represents the photothermal conversion efficiency (PCE), h is the heat transfer coefficient, A represents the surface area of the sample cell. T_{\max} and T_{surr} are the maximum temperature of PTM-AIEsomes solution and the surrounding temperature, respectively. I represent incident laser power. A_{808} is the absorbance of PTM-AIEsomes at 808 nm. The value of hA can be calculated according to the following Eq. (2),

$$hA = \frac{mC_{\text{water}}}{\tau_s} \quad (2)$$

Where C_{water} represents the heat capacity of the solution used to dissolve the samples, m is the mass of the solution. τ_s is a system time constant.

Q_{dis} is the heat dissipation from the laser absorbed by the solvent and the sample cell which was measured independently to be 0.03554 (808 nm), according to the following Eq. (3),

$$Q_{\text{dis}} = \frac{mC_{\text{water}}(T_{\max(\text{water})} - T_{\text{surr}})}{\tau_{\text{water}}} \quad (3)$$

The PCE (η) of PTM-AIEsomes under 808 nm laser irradiation was 20.73%.

Photothermal performance of AIEsomes and PTM-AIEsomes upon laser irradiation

To evaluate the photothermal performance, aqueous solutions of AIEsomes and PTM-AIEsomes were irradiated with an 808 nm laser continuously for 10 min. The temperature change was monitored every second using a digital thermometer that was equipped with a thermocouple probe. For testing of photothermal stability, the photothermal heating of PTM-AIEsomes solution was measured during five circles of heating and cooling by turning on and off the incident laser. To directly observe the photothermal heating, infrared thermographic maps of PTM-AIEsomes in aqueous solution upon 808 nm laser irradiation were recorded by an infrared camera (FLIR E54) and quantified with FLIR software.

Motile behaviors of AIEsomes and PTM-AIEsomes

Nanosight Tracking Analysis (NTA) was conducted to evaluate the motile behavior of AIEsomes and PTM-AIEsomes in response to laser irradiation by a Nanosight NS300 equipped with sCMOS camera and external laser source (808 nm, UltraLasers). Briefly, 1 mL of diluted sample was loaded in the NTA sample chamber using a syringe (1 mL, without needle). The approximate concentration of AIEsomes and PTM-AIEsomes were 4.81×10^8 and 1.4×10^8 particles mL^{-1} , respectively. The NTA 2.2 software allows the extract and track the motion trajectory of single nanoparticles. The motion of AIEsomes and PTM-AIEsomes was recorded by NTA for 30 s. Two-dimensional extraction of coordinates (x , y) was obtained by recording the trajectories of the polymersomes. The MSD of each AIEsome or PTM-AIEsome was calculated using the following Eq. (4)⁷⁰,

$$\text{MSD} = [\Delta r^2(t)] = \left[\frac{1}{N} \sum_{i=0}^N (r_i(t) - r_i(0))^2 \right] \quad (4)$$

Where r represents radius, t is sampling time, and $\text{MSD}(t) = 2dD$. Here, D is the diffusion coefficient and d is the dimensionality (NTA measurements have dimension $d=2$). The equation $\text{MSD} = (4D)\Delta t + \langle V^2$

(Δt^2) was used to fit the MSD curves. From the MSD fitting curves, the motile behavior of the AIEsomes or PTM-AIEsomes could be determined. According to the Golestanian's self-diffusiophoretic model⁴⁶, a linear MSD curve can be obtained if the polymersome samples are in Brownian motion. Under this situation, the equation used for extracting MSD should be $\text{MSD} = (4D)\Delta t$ ⁶⁹. Nonlinear MSD fitting curve was obtained when the polymersome samples exhibited self-propelled motion. Average velocity of polymersome samples was extracted from the fitting of the average MSD curves, according to the reported method^{70,71}.

Data availability

Additional data supporting the findings of this work are available from the corresponding author upon request. Source data are provided with this paper in the Source Data file. Source data are provided with this paper.

References

- Napoli, A. et al. Oxidation-responsive polymeric vesicles. *Nat. Mater.* **3**, 183–189 (2004).
- Discher, B. M. et al. Polymersomes: tough vesicles made from diblock copolymers. *Science* **284**, 1143–1146 (1999).
- Discher, D. E. & Ahmed, F. Polymersomes. *Annu. Rev. Biomed. Eng.* **8**, 323–341 (2006).
- Gaitzsch, J., Huang, X. & Voit, B. Engineering functional polymer capsules toward smart nanoreactors. *Chem. Rev.* **116**, 1053–1093 (2016).
- Zelmer, C. et al. Organelle-specific targeting of polymersomes into the cell nucleus. *Proc. Natl. Acad. Sci. USA* **117**, 2770–2778 (2020).
- Guinart, A. et al. Synthetic molecular motor activates during delivery from polymersomes. *Proc. Natl. Acad. Sci. USA* **120**, e2301279120 (2023).
- Scheerstra, J. F. et al. Polymersomes as a potential platform for cancer immunotherapy. *Mater. Today Adv.* **13**, 100203 (2022).
- Wong, C. K. et al. Formation of non-spherical polymersomes driven by hydrophobic directional aromatic perylene interactions. *Nat. Commun.* **8**, 1240 (2017).
- Ruiz-Pérez, L. et al. Molecular engineering of polymersome surface topology. *Sci. Adv.* **2**, e1500948 (2016).
- Miller, A. J. et al. Probing and tuning the permeability of polymersomes. *ACS Cent. Sci.* **7**, 30–38 (2021).
- Zhu, Y. et al. Recent advances in permeable polymersomes: fabrication, responsiveness, and applications. *Chem. Sci.* **14**, 7411–7437 (2023).
- Fielden, S. D. P. et al. Triggered polymersome fusion. *J. Am. Chem. Soc.* **145**, 5824–5833 (2023).
- Belluati, A. et al. Artificial cell synthesis using biocatalytic polymerization-induced self-assembly. *Nat. Chem.* **16**, 564–574 (2024).
- Zhao, Z. et al. Recent progress in polymerization-induced self-assembly: from the perspective of driving forces. *Aggregate* **5**, e418 (2024).
- Meeuwissen, S. A. et al. Controlled shape transformation of polymersome stomatocytes. *Angew. Chem. Int. Ed.* **50**, 7070–7073 (2011).
- Salva, R. et al. Polymersome shape transformation at the nanoscale. *ACS Nano* **7**, 9298–9311 (2013).
- Balasubramanian, V. et al. Multifaceted polymersome platforms: spanning from self-assembly to drug delivery and protocells. *Prog. Polym. Sci.* **60**, 51–58 (2016).
- Gao, Y. et al. Physically and chemically compartmentalized polymersomes for programmed delivery and biological applications. *Biomacromolecules* **24**, 5511–5538 (2023).
- Kim, K. T. et al. Polymersome stomatocytes: controlled shape transformation in polymer vesicles. *J. Am. Chem. Soc.* **132**, 12522–12524 (2010).

20. Rikken, R. S. M. et al. Shaping polymersomes into predictable morphologies via out-of-equilibrium self-assembly. *Nat. Commun.* **7**, 12606 (2016).
21. Li, X. F., Wang, Y. X. & Yan, Q. Cyanine polymersomes in breathe gas signaling molecule: SO₂-driven bilayer tubular deformation for transmembrane traffic regulation. *Angew. Chem. Int. Ed.* **62**, e202305290 (2023).
22. Wong, C. K. et al. Dynamic metastable polymersomes enable continuous flow manufacturing. *Nat. Commun.* **14**, 6237 (2023).
23. Jung, M. et al. Vesicle-polymer hybrid architectures: a full account of the parachute architecture. *Langmuir* **16**, 3165–3174 (2000).
24. Shao, J. et al. Photoactivated polymersome nanomotors: traversing biological barriers. *Angew. Chem. Int. Ed.* **59**, 16918–16925 (2020).
25. Vutukuri, H. R. et al. Active particles induce large shape deformations in giant lipid vesicles. *Nature* **586**, 52–56 (2020).
26. Rinaldin, M. et al. Geometric pinning and antimixing in scaffolded lipid vesicles. *Nat. Commun.* **11**, 4314 (2020).
27. Joseph, A. et al. Chemotactic synthetic vesicles: design and applications in blood-brain barrier crossing. *Sci. Adv.* **3**, e1700362 (2017).
28. De Yoreo, J. J. & Sommerdijk, N. A. J. M. Investigating materials formation with liquid-phase and cryogenic TEM. *Nat. Rev. Mater.* **1**, 16035 (2016).
29. Ianiro, A. et al. Liquid-liquid phase separation during amphiphilic self-assembly. *Nat. Chem.* **11**, 320–328 (2019).
30. Rizvi, A. et al. Nonionic block copolymer coacervates. *Macromolecules* **53**, 6078–6086 (2020).
31. Wong, C. K. et al. Vesicular polymer hexosomes exhibit topological defects. *J. Am. Chem. Soc.* **142**, 10989–10995 (2020).
32. Rizvi, A. & Patterson, J. P. Liquid-liquid phase separation induced auto-confinement. *Soft Matter* **20**, 1978–1982 (2024).
33. Rizvi, A. et al. A close look at molecular self-assembly with the transmission electron microscope. *Chem. Rev.* **121**, 14232–14280 (2021).
34. Cao, S. et al. Photoactivated nanomotors via aggregation induced emission for enhanced phototherapy. *Nat. Commun.* **12**, 2077 (2021).
35. Luo, Y. T. et al. Polymer vesicles with integrated photothermal responsiveness. *J. Am. Chem. Soc.* **145**, 20073–20080 (2023).
36. Liu, S. J. et al. Constitutional isomerization enables bright NIR-II AIEgen for brain-inflammation imaging. *Adv. Funct. Mater.* **30**, 1908125 (2020).
37. Luo, Y. T. et al. Acrylate-substituted thiadiazoloquinoxaline yields ultralow band gap (0.56 eV) conjugated polymers for efficient photoacoustic imaging. *ACS Appl. Polym. Mater.* **3**, 3247–3253 (2021).
38. Liu, S. J. et al. Molecular motion in aggregates: manipulating TICT for boosting photothermal theranostics. *J. Am. Chem. Soc.* **141**, 5359–5368 (2019).
39. Wang, J. X. et al. AIEgen-based polymer nanocomposites for imaging-guided photothermal therapy. *ACS Appl. Polym. Mater.* **2**, 4306–4318 (2020).
40. Kita-Tokarczyk, K. et al. Block copolymer vesicles—using concepts from polymer chemistry to mimic biomembranes. *Polymer* **46**, 3540–3563 (2005).
41. van den Akker, W. P. et al. Nonlinear transient permeability in pH-responsive bicontinuous nanospheres. *J. Am. Chem. Soc.* **145**, 8600–8608 (2023).
42. Cao, S. P. et al. Cucurbit-like polymersomes with aggregation-induced emission properties show enzyme-mediated motility. *ACS Nano* **15**, 18270–18278 (2021).
43. Mortazavifar, A., Raissi, H. & Akbari, A. DFT and MD investigations on the functionalized boron nitride nanotube as an effective drug delivery carrier for carmustine anticancer drug. *J. Mol. Liq.* **276**, 577–587 (2019).
44. Jones, R. O. Density functional theory: its origins, rise to prominence, and future. *Rev. Mod. Phys.* **87**, 897 (2015).
45. Hinuma, Y. et al. Comparison of approximations in density functional theory calculations: energetics and structure of binary oxides. *Phys. Rev. B* **96**, 094102 (2017).
46. Mao, Y. Z. et al. From intermolecular interaction energies and observable shifts to component contributions and back again: a tale of variational energy decomposition analysis. *Annu. Rev. Phys. Chem.* **72**, 641–666 (2021).
47. Wu, H. L. et al. Studying reaction mechanisms in solution using a distributed electron microscopy method. *ACS Nano* **15**, 10296–10308 (2021).
48. Wu, H. L. et al. Liquid-phase electron microscopy for soft matter science and biology. *Adv. Mater.* **32**, 2001582 (2020).
49. van Omme, J. T. et al. Liquid phase transmission electron microscopy with flow and temperature control. *J. Mater. Chem. C* **8**, 10781–10790 (2020).
50. Wu, H. L. et al. Understanding, mimicking and mitigating radiolytic damage to polymers in liquid phase transmission electron microscopy. *Adv. Mater.* **36**, e2402987 (2024).
51. Lu, T. & Spruijt, E. Multiphase complex coacervate droplets. *J. Am. Chem. Soc.* **142**, 2905–2914 (2020).
52. Chen, C. et al. A Janus Au-polymersome heterostructure with near-field enhancement effect for implant-associated infection phototherapy. *Adv. Mater.* **35**, 2207950 (2023).
53. Liu, Z. et al. Janus nanoparticles targeting extracellular polymeric substance achieve flexible elimination of drug-resistant biofilms. *Nat. Commun.* **14**, 5132 (2023).
54. Howse, J. R. et al. Self-motile colloidal particles: from directed propulsion to random walk. *Phys. Rev. Lett.* **99**, 048102 (2007).
55. Huang, X. et al. Photoactivated organic nanomachines for programmable enhancement of antitumor efficacy. *Small* **18**, 2201525 (2022).
56. Li, J. X. et al. Micro/nanorobots for biomedicine: delivery, surgery, sensing, and detoxification. *Sci. Robot.* **2**, eaam6431 (2017).
57. Gao, X. Y. et al. Visualization and quantification of cellular RNA production and degradation using a combined fluorescence and mass spectrometry characterization assay. *Chem. Commun.* **55**, 8321–8324 (2019).
58. Cao, S. P. et al. Biodegradable polymersomes with structure inherent fluorescence and targeting capacity for enhanced photodynamic therapy. *Angew. Chem. Int. Ed.* **60**, 17629–17637 (2021).
59. Kremer, J. R. et al. Computer visualization of three-dimensional image data using IMOD. *J. Struct. Biol.* **116**, 71–76 (1996).
60. Schrödinger, Inc. *User Manual*. <http://www.schrodinger.com> (New York, NY, 2023).
61. Lu, C. et al. OPLS4: improving force field accuracy on challenging regimes of chemical space. *J. Chem. Theory Comput.* **17**, 4291–4300 (2021).
62. Mohamadi, F. et al. MacroModel—An integrated software system for modeling organic and bioorganic molecules using molecular mechanics. *J. Comput. Chem.* **11**, 440–467 (1990).
63. Bowers, K. J. et al. Scalable algorithms for molecular dynamics simulations on commodity clusters. In *Proc. 2006 ACM/IEEE conference on Supercomputing*. 84-es (Association for Computing Machinery, 2006).
64. Andersen, H. C. et al. Molecular dynamics simulations at constant pressure and/or temperature. *J. Chem. Phys.* **72**, 2384–2393 (1980).
65. Bochevarov, A. D. et al. Jaguar: a high-performance quantum chemistry software program with strengths in life and materials sciences. *Int. J. Quantum Chem.* **113**, 2110–2142 (2013).
66. Grimme, S. et al. A consistent and accurate ab initio parametrization of density functional dispersion correction (DFT-D) for the 94 elements H–Pu. *J. Chem. Phys.* **132**, 154104 (2010).

67. Hay, P. J. & Wadt, W. R. Ab initio effective core potentials for molecular calculations. Potentials for K to Au including the outermost core orbitals. *J. Chem. Phys.* **82**, 299–310 (1985).
68. Marten, B. et al. New model for calculation of solvation free energies: Correction of self-consistent reaction field continuum dielectric theory for short-range hydrogen-bonding effects. *J. Phys. Chem.* **100**, 11775–11788 (1996).
69. Liu, C. et al. A water-soluble, NIR-absorbing quaterylene diimide chromophore for photoacoustic imaging and efficient photo-thermal cancer therapy. *Angew. Chem. Int. Ed.* **58**, 1638–1642 (2019).
70. Pijpers, I. A. B. et al. Hybrid biodegradable nanomotors through compartmentalized synthesis. *Nano Lett.* **20**, 4472–4480 (2020).
71. Nijemeisland, M. et al. A compartmentalized out-of-equilibrium enzymatic reaction network for sustained autonomous movement. *ACS Cent. Sci.* **2**, 843–849 (2016).

Acknowledgements

This work was financially supported by the Netherlands Ministry of Education, Culture and Science (Gravitation Program Interactive Polymer Materials, 024.005.020) to J.C.M.H., the Spinoza premium SPI 71-259 to J.C.M.H., and the European Union's Horizon 2020 research and innovation program Marie Skłodowska-Curie Innovative Training Network (ITN) Nanomed (No. 676137) to J.C.M.H. Y.L. appreciates the support from the China Scholarship Council. Author 1, Author 2, and Author 3 contributed equally to this work. DIFFER is part of the institutes organization of NWO. This work was sponsored by NWO Exact and Natural Sciences for the use of supercomputer facilities.

Author contributions

J.S., Y.L. and H.W. contributed equally to this work. J.S., Y.L. and H.W. wrote the manuscript; J.S., Y.L., H.W., L.K.E.A.A. and J.C.M.H. designed the research; J.S., Y.L., H.W., J.W., S.C. and H.S. performed the experiments; H.W. performed cryo-TEM, cryo-ET, and LP-TEM experiments; J.S., Y.L., H.W., J.W., S.C., H.S. and H.Z. collected and analyzed the data; H.H.P.G., H.Z. and H.F. discussed the cryo-TEM, cryo-ET, and LP-TEM data; X.Z. conducted the DFT and MD simulations; S.E. discussed the DFT and MD simulations data. All the authors contributed to the critical discussion and implications.

Competing interests

The authors declare no competing interests.

Additional information

Supplementary information The online version contains supplementary material available at <https://doi.org/10.1038/s41467-025-57711-y>.

Correspondence and requests for materials should be addressed to Loai K. E. A. Abdelmohsen or Jan C. M. van Hest.

Peer review information *Nature Communications* thanks the anonymous reviewers for their contribution to the peer review of this work. A peer review file is available.

Reprints and permissions information is available at <http://www.nature.com/reprints>

Publisher's note Springer Nature remains neutral with regard to jurisdictional claims in published maps and institutional affiliations.

Open Access This article is licensed under a Creative Commons Attribution-NonCommercial-NoDerivatives 4.0 International License, which permits any non-commercial use, sharing, distribution and reproduction in any medium or format, as long as you give appropriate credit to the original author(s) and the source, provide a link to the Creative Commons licence, and indicate if you modified the licensed material. You do not have permission under this licence to share adapted material derived from this article or parts of it. The images or other third party material in this article are included in the article's Creative Commons licence, unless indicated otherwise in a credit line to the material. If material is not included in the article's Creative Commons licence and your intended use is not permitted by statutory regulation or exceeds the permitted use, you will need to obtain permission directly from the copyright holder. To view a copy of this licence, visit <http://creativecommons.org/licenses/by-nc-nd/4.0/>.

© The Author(s) 2025